doi: 10.82124/CEAS-GNC-2026-026

Trim analysis of a three-line kite airborne wind energy system using bifurcation analysis

Kevin Yu
Undergraduate Student, University of Bristol, Bristol, United Kingdom
2003kevinyu@gmail.com

Duc H. Nguyen
Lecturer in Flight Dynamics and Control, University of Bristol, Bristol, United Kingdom
duc.nguyen@bristol.ac.uk *(corresponding author)*

Iván Castro-Fernández
Tenure researcher, Department of Space Programmes, Instituto Nacional de Técnica Aeroespacial, Carretera de Ajalvir Km. 4, 28850 Torrejón de Ardoz, Madrid, Spain
ivancastrofernandez95@gmail.com

Francisco DeLosRíos-Navarrete
Department of Aerospace Engineering, Universidad Carlos III de Madrid, Avenida de la Universidad 30, 28911 Leganés, Madrid, Spain.
francisco.los@alumnos.uc3m.es

Jorge González-García
PhD Student, Department of Aerospace Engineering, Universidad Carlos III de Madrid, Avenida de la Universidad 30, 28911 Leganés, Madrid, Spain
jorgegga@ing.uc3m.es

Mark H. Lowenberg
Professor of Flight Dynamics, University of Bristol, Bristol, United Kingdom
m.lowenberg@bristol.ac.uk

Gonzalo Sánchez-Arriaga
Full Professor, Department of Aerospace Engineering, Universidad Carlos III de Madrid, Avenida de la Universidad 30, 28911 Leganés, Madrid, Spain
gonsanch@ing.uc3m.es

ABSTRACT

Kites possess complex flying characteristics that must be understood to ensure efficient operation in airborne wind energy applications. The flight dynamics of a six-degrees-of-freedom three-line delta kite with full tether dynamics through a spring-mass model is investigated. Results reveal nonlinear behaviours that agree with prior analyses on simpler models of single-tether systems with constrained dynamics. These include the co-existence of multiple steady-state solutions at low airspeeds and a pendulum-mode instability that puts the kite in an 'automatic' figure-of-eight trajectory without any active control input. In the three-line system studied, this figure-of-eight trajectory is identified to be a stable limit cycle, which is influenced by the lateral distance between the left and right tether anchor points on the ground station. Increasing this distance stabilises the pendulum mode, which destroys the limit cycle and puts the kite in a stable trim condition. However, doing so results in excessive lateral stability, thereby reducing the manoeuvrability of the kite. This finding highlights the impact of ground station design on kite flight dynamics and underlines a trade-off between stability and manoeuvrability.

Keywords: airborne wind energy, kite, tether, nonlinear dynamics, bifurcation, renewable energy

Nomenclature

C_x, C_y, C_z = body-axis force coefficients
C_l, C_m, C_n = body-axis roll, pitch, and yaw moment coefficients
D_{LR} = lateral distance between side tether anchor points
H = height (= – z_E)
L_C, L_L, L_R = central, left, and right tether lengths
L_0 = nominal tether length
$\boldsymbol{x_s}$ = state vector
$\boldsymbol{x_c}$ = control vector
x_E, y_E, z_E = Earth-axis coordinates
x_B, y_B, z_B = Body-axis coordinates
α = angle of attack
β = sideslip angle
ΔL_P = simultaneous side tether length input for pitch control
ΔL_S = differential side tether length input for lateral control
λ = continuation parameter
ϕ, θ, ψ = Euler angles (roll, pitch, yaw)

1 Introduction

Airborne wind energy (AWE) is an emerging technology for renewable energy. Unlike conventional wind turbines, AWE uses a tethered flying device to generate electricity at high altitudes. In the ground-gen configuration, the mechanical power delivered by the tether tension is transformed into electrical power by a generator on the ground. AWE systems have higher capacity factor than conventional wind turbines, in addition to being able to relocate and having lower lifetime material usage. An overview of AWE technology can be found in [1, 2].

Soft kites, hybrid kites, and fixed-wing aircraft are three of the most popular choices for the aerial component of AWE. Kites offer a lightweight platform with higher damage tolerance in the event of crashes compared to fixed-wing aircraft. Previous studies have uncovered nonlinear behaviours in kites, such as the co-existence of multiple equilibrium and periodic solutions at low wind speeds [3-5] and unstable pendulum-mode oscillations that resemble a figure-of-eight trajectory [6] (although the configuration used in [6] was an inflatable fixed-wing aircraft – arguably a hybrid between kites and fixed-wing aircraft). Some of these results have been verified with wind tunnel data [5, 7]. The fidelity of these nonlinear kite dynamics studies has also increased over the years. While early work assumed a rigid and drag-less tether, and constrained the dynamics to two [4] and five [6] degrees of freedom (DoF), recent studies have analysed the stability of kite systems, where the aerial component has full 6 DoF [8]. With the recent introductions of several advanced AWE simulators that includes full tether dynamics [9-14], there is a need to adapt the prior stability analyses to these combined kite/tether systems. In a simulation environment, each elastic tether line increases the number of states significantly, resulting in higher computational cost. For instance, the stability characteristics of the three-line kite configuration has remained largely unexplored at an academic level. Further investigations into this area could benefit future AWE design, considering Enerkite's adoption of the three-line configuration on its AWE system [15].

Another key aspect in AWE simulations is the aerodynamic model employed to obtain the aerodynamic forces and moments on the kite. It greatly influences the motion of the kite and power predictions during typical AWE trajectories, and the appearance and stability of equilibrium states. As recently highlighted in a review on AWE aerodynamics [16], many prior works on kite dynamics and control used simple aerodynamic models based on constant aerodynamic coefficients and/or constant aerodynamic efficiency. Higher-degree-of-freedom simulations largely relied on models based on constant aerodynamic stability derivatives that were generally estimated either from empirical or heuristic data. Only a few of them used mid- and high-fidelity aerodynamic tools such as potential-flow models and computational fluid dynamics to estimate these aerodynamic derivatives [17, 18]. Indeed, recent studies suggest that these simple aerodynamic models when estimated with reliable aerodynamic tools are virtually equivalent to the direct coupling between the aerodynamic tool and the dynamic simulator [19]. These models may include steady terms if they are dependent only on the angle of attack and sideslip angle, and quasi-steady terms by including the dependence on the angular rates. The latter are well-known to highly influence the stability of equilibria [8].

This work focuses on analysing the nonlinear flight dynamics of a rigid-frame three-line delta kite AWE system, which combines a rigid frame with a membrane canopy. Numerical analysis is done on a MATLAB simulator built on top of the LAgrangian Kite SimulAtor (LAKSA) package [12, 20] featuring 6 DoF, full tether dynamics through a spring-mass model, and realistic aerodynamics and inertia properties. Furthermore, the aerodynamic model used in this study is based on aerodynamic stability derivatives derived from a three-dimensional unsteady panel method that, for the force coefficients, fits previous experimental data reasonably [21]. The aerodynamic and tether models provide the foundation for investigating the kite's static and dynamic stability properties. In particular, equilibrium trim points and limit cycles are calculated using the Dynamical Systems Toolbox [22] – a MATLAB implementation of the numerical continuation software AUTO [23]. Results focus on the kite's open-loop dynamics at different wind speeds and tether anchor arrangements on the ground station, which uncovers nonlinear behaviours similar to those reported in previous studies that used simplified models [3-7] and highlight the role of ground station design on kite's stability.

2 Methodology

2.1 Simulation framework

The MATLAB-based simulator used in this paper is referred to as KiteElastic3 [24, 25], which is a modification of the KiteElastic module in the LAKSA open-source software [20, 26]. Unlike other modules of LAKSA, KiteElastic3 features a Newtonian formulation and uses dimensional variables. The kite is modelled as a rigid body with 6 degrees of freedom. Its dynamics is studied with respect to an inertial Earth frame with origin at the ground station (shown schematically in Fig. 3), the x_E-axis pointing opposite the wind velocity, the z_E-axis pointing toward the Earth's centre, and the y_E-axis completing the right-hand frame (see Fig. 1a). This arrangement results in x_E and y_E axes spanning the assumed flat ground, and the kite's height $H = -z_E$.

The KiteElastic3 simulator models the three-line kite AWE system built by the University Carlos III of Madrid (UC3M), which is shown in Fig. 2a. The kite is a rigid-frame delta kite of 3.66 m wingspan, with geometry based on the commercial HQ Fazer XXL kite. The UC3M's kite has a total mass with avionics of 2 kg. Table I summarises the physical parameters of the kite and the tethers. To connect the three main tethers – labelled L_L, L_C, and L_R – a series of eight bridle lines are used. The bridle-kite connection points are fixed in the body frame that originates from the kite's centre of mass, the x_B-axis along the central spine of the kite, the z_B-axis normal to it and contained in the plane of symmetry of the kite pointing downwards in normal flight condition, and the y_B-axis completing the right-handed frame (see Fig. 1b). Fig. 2a shows the location of the eight connection points on the kite, and

Table II lists their coordinates in the body frame, along with the length of the bridle between each of them and the attachment points with the tethers.

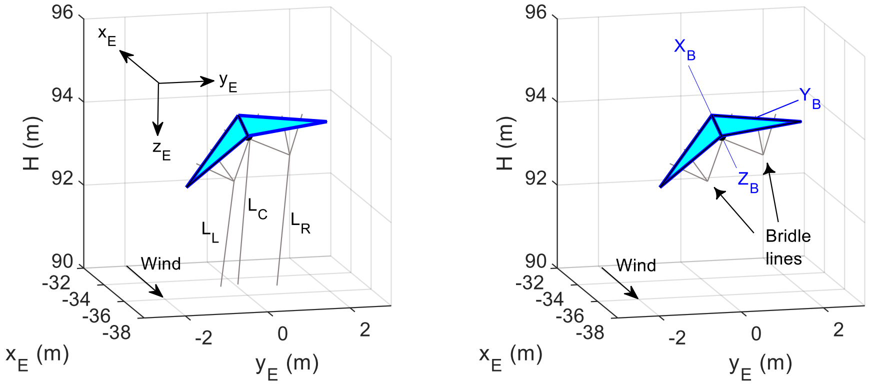

(a) (b)

Fig. 1. Visualisation of the kite, bridle and tethers in the Earth's frame. Panel (a) shows the three main tether lines, and panel (b) shows the body-axis reference system. All results assume a steady wind field pointing in the negative-x_E direction.

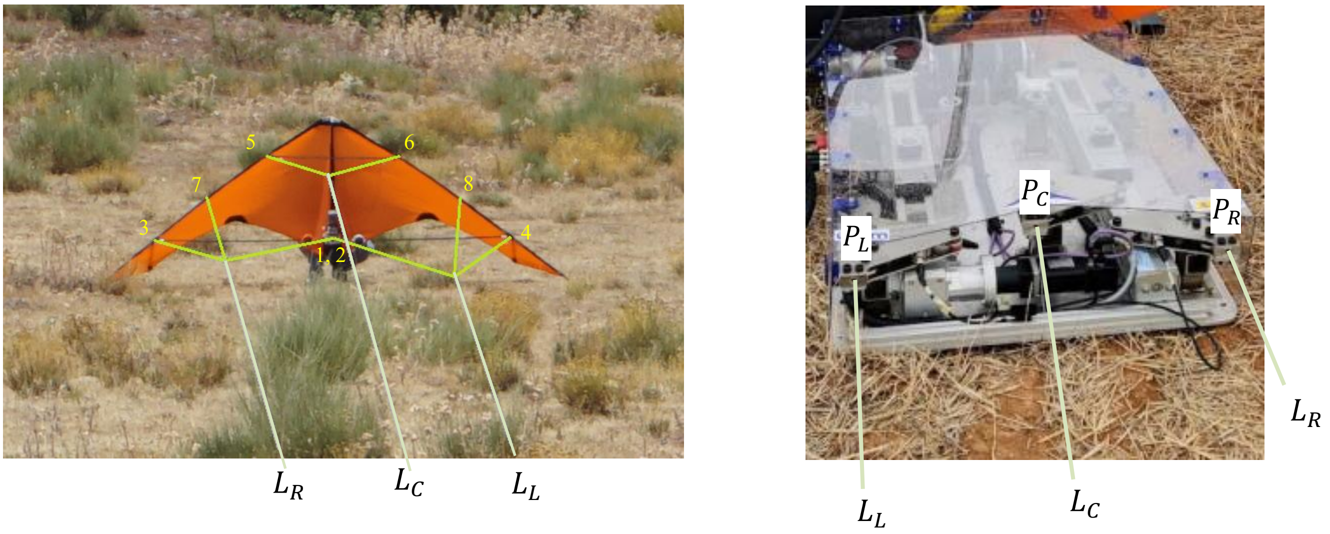

(a) (b)

Fig. 2. The UC3M kite (a) and the three-line tether control system (b). Bridle lines (yellow) and tether lines (green) are highlighted.

Flight control is achieved by changing the lengths of the three tethers (L_L, L_C, L_R), which are connected to a ground station pictured in Fig. 2b. The tether-ground station connection points (referred to as anchor points) are labelled P_L, P_C, and P_R as shown in Fig. 2b and Fig. 3. Their Earth-axis coordinates are listed in Table III. To denote the lateral distance between the left and right anchor points, a parameter called D_{LR} is used as shown in Fig. 3. This parameter has a considerable effect on dynamic stability of the kite as discussed in section 3.2.

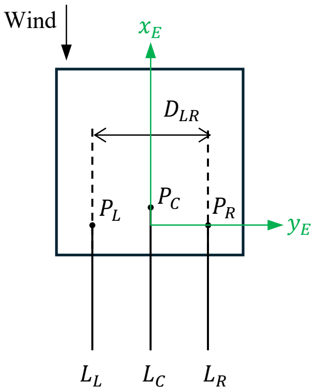

Fig. 3. Top-down schematic of the ground station with its tether anchor points shown.

Table I. Physical parameters of the kite and tether.

Kite	
Mass	2 kg
Mean aerodynamic chord c	0.6 m
Wingspan b	3.66 m
Wing area S	1.87 m^2
Moment of inertia I_x	0.715 kg m^2
Moment of inertia I_y	0.115 kg m^2
Moment of inertia I_z	0.819 kg m^2
Moment of inertia I_{xz}	0 kg m^2

Tether	
Radius	1 mm
Linear density	0.0018 kg/m
Young's modulus	980 GPa
Damping coefficient	350 N s/m
Drag coefficient	1.1
Nominal tether length L_0	100 m
Central tether length L_C	100.535 m

Table II. Body-axis coordinates of the kite-bridle connection points and the corresponding bridle lengths.

Point	x_B (m)	y_B (m)	z_B (m)	Bridle length (m)
1	−0.083	0	0.015	1.219
2	−0.083	0	0.015	1.219
3	−0.083	1.38	0.015	1.17
4	−0.083	−1.38	0.015	1.17
5	0.406	0.45	0.015	0.731
6	0.406	−0.45	0.015	0.731
7	0.1	0.93	0.015	1.073
8	0.1	−0.93	0.015	1.073

Table III. Earth-axis coordinates of the three tether anchor points at the ground station.

Anchor point	x_E (m)	y_E (m)	z_E (m)
P_L	0	$-D_{LR}/2$	0
P_R	0	$D_{LR}/2$	0
P_C	0.05	0	0

The open-loop equations of motion are represented by a system of ordinary differential equations in the form of

$$\dot{\boldsymbol{x}}_{\boldsymbol{s}} = \boldsymbol{f}(\boldsymbol{x}_{\boldsymbol{s}}, \boldsymbol{x}_{\boldsymbol{c}}), \tag{1}$$

where $\boldsymbol{x}_{\boldsymbol{s}}$ and $\boldsymbol{x}_{\boldsymbol{c}}$ are the state and control vectors, respectively. $\boldsymbol{x}_{\boldsymbol{s}}$ has dimension $13+3\times6\times N$, comprising the 13 rigid-body states describing the kite's 6 DoF motion, considering quaternions to describe its angular state, and $3\times6\times N$ states describing the 3 tethers. Each tether is discretised into N nodes, which are identified by their Cartesian-coordinate positions (3 states each) and velocities (also 3 states each). The nodes are linked by mass-spring-damper elements. The bridles are also modelled as elastic tethers with the same characteristic of the three main tethers. Aerodynamic, elastic, and gravitational forces act on tether segments, which are bounded by one node on each end. All results in this paper use $N = 10$, bringing the number of states in the simulator to 193. The flow $\boldsymbol{f}$ in Eq. (1) is obtained by writing the kinematic and dynamic equations for the 3N particles used to discretize the tether and the kite, which is a rigid body. For brevity, the explicit form of $\boldsymbol{f}$ is not given here, but it can be found in Ref. [27], and the code is available in the public repository of LAKSA [25]. Nonetheless, some important aspects of the model that are important to understand this work are given presented below.

To describe the kite's dynamics, the total force $\boldsymbol{F}_K$ and torque $\boldsymbol{M}_K$ in the body axis are needed. They can be calculated as follows

$$\begin{gathered} \boldsymbol{F}_K = \boldsymbol{F}_A + \boldsymbol{F}_T + \boldsymbol{F}_W, \\ \boldsymbol{M}_K = \boldsymbol{M}_A + \boldsymbol{M}_T, \end{gathered} \tag{2}$$

where the subscripts A, T, and W denote contributions from aerodynamics, tether, and gravity, respectively. Further details on the components making up the aerodynamic force and torque are described in section 2.2. From here, the standard rigid-body 6 DoF translational and rotational equations of motion derived from Newton's second law can be used to calculate the kite's trajectory and attitude.

The control vector $\boldsymbol{x}_{\boldsymbol{c}}$ in Eq. (1) contains three elements: the lengths of the two side tethers L_L and L_R, and the central tether length L_C. Steering forces are generated by creating a difference in length between the two side tethers (for example, lengthening the left tether while shortening the right one), while pitch control is achieved by changing both side-tether lengths simultaneously. The tether lengths are written as

$$\begin{gathered} L_L = L_0 + \Delta L_P - \Delta L_S, \\ L_R = L_0 + \Delta L_P + \Delta L_S, \\ L_C = L_0, \end{gathered} \tag{3}$$

where $L_0 = 100$ m is a nominal length, ΔL_P is the simultaneous side-tether length change for pitch control, and ΔL_S is the differential length input of the two side tethers for steering control. The chosen ΔL_S signs in the L_L and L_R equations are consistent with the sign convention for ailerons in conventional aircraft, so that a positive ΔL_S input results in a left-wing-down rolling moment.

2.2 Aerodynamic model

The aerodynamic forces and moments of the delta kite are given by a simple analytical model based on constant aerodynamic stability derivatives. The latter were found by using an in-house three-dimensional Unsteady Panel Method (UnPaM) [28] based on potential flow. UnPaM was already applied to the same delta kite and compared to experimental data in previous works [21, 29]. It provided a reasonable accuracy in the lift and lateral force coefficients for a wide range of angles of attack $\alpha \in [20°, 40°]$ and sideslip angles $\beta \in [-10°, 10°]$, whereas it underestimated the drag coefficient due to the lack of viscous effects. The moment coefficients provided by UnPaM were of the same order as the experimental ones, but it was difficult to establish a quantitative comparison due to the presence of experimental uncertainties in the estimation of the experimental moments [21]. The zero-lift angle of attack computed with UnPaM resulted in about 15°. Since no stall is expected around this value, the potential-flow model is considered accurate for $\alpha \in [10°, 40°]$.

Considering these limitations and validity ranges for α and β, the model computes the aerodynamic force ($\boldsymbol{F}_A$) and moment ($\boldsymbol{M}_A$) around the centre of mass as

$$\begin{aligned} \boldsymbol{F}_A &= \frac{1}{2}\rho S V_A^2 (C_X\, \boldsymbol{i}_B + C_Y\, \boldsymbol{j}_B + C_Z\, \boldsymbol{k}_B), \\ \boldsymbol{M}_A &= \frac{1}{2}\rho S V_A^2 (b\, C_l\, \boldsymbol{i}_B + c\, C_m\, \boldsymbol{j}_B + b\, C_n\, \boldsymbol{k}_B), \end{aligned} \tag{4}$$

where S, b and c are the area, wingspan and mean aerodynamic chord of the kite (see Table I), and

$$\boldsymbol{V}_A = \boldsymbol{V}_G - \boldsymbol{V}_W, \tag{5}$$

is the aerodynamic velocity of the kite with $\boldsymbol{V}_G$ and $\boldsymbol{V}_W$ its absolute velocity and the wind velocity at the kite's height, respectively. The angle of attack and sideslip angles are defined as

$$\begin{aligned} \alpha &= \arctan\left(\frac{\boldsymbol{V}_A \cdot \boldsymbol{k}_B}{\boldsymbol{V}_A \cdot \boldsymbol{i}_B}\right), \\ \beta &= \arcsin\left(\frac{\boldsymbol{V}_A \cdot \boldsymbol{j}_B}{V_A}\right). \end{aligned} \tag{6}$$

The aerodynamic coefficients as a function of the angle of attack α, the sideslip angle β, and the angular velocity vector, $\boldsymbol{\omega}_{BE} = \omega_X\, \boldsymbol{i}_B + \omega_Y\, \boldsymbol{j}_B + \omega_Z\, \boldsymbol{k}_B$, read

$$\begin{aligned} C_X &= C_{X0} + C_{X\alpha}\, \alpha, \\ C_Y &= C_{Y\beta}\, \beta, \\ C_Z &= C_{Z0} + C_{Z\alpha}\, \alpha, \\ C_l &= C_{l\beta}\, \beta + C_{lp}\, p, \\ C_m &= C_{m0} + C_{m\alpha}\, \alpha + C_{mq}\, q, \\ C_n &= C_{n\beta}\, \beta + C_{nr}\, r, \end{aligned} \tag{7}$$

where $p = \frac{\omega_X\, b}{2\, V_{Ref}}$, $q = \frac{\omega_Y\, c}{V_{Ref}}$, $r = \frac{\omega_Z\, b}{2\, V_{Ref}}$ are the nondimensional angular velocity components, $V_{Ref} = 10\ \mathrm{m/s}$ is a constant reference velocity and $C_{X0}, C_{X\alpha}, C_{Y\beta}$, etc. are the constant aerodynamic stability derivatives given by the numerical tool UnPaM. Their values are given in Table IV.

Table IV. Aerodynamic stability derivatives of the analytical aerodynamic model based on UnPaM.

Aerodynamic stability derivative	Value
C_{X0}	−0.95
$C_{X\alpha}$	2.55
$C_{Y\beta}$	−0.37
C_{Z0}	0.85
$C_{Z\alpha}$	−3.53
$C_{l\beta}$	0.021

Aerodynamic stability derivative	Value
C_{lp}	−0.074
C_{m0}	0.17
$C_{m\alpha}$	0.21
C_{mq}	0.32
$C_{n\beta}$	0.09
C_{nr}	0.018

The estimation of these parameters was performed by linearizing UnPaM's results about a nominal angle of attack $\alpha_0 = 30°$ and sideslip angle $\beta_0 = 0°$, which is an intermediate aerodynamic condition within the validity range for α and β, and above the angle of attack of the zero-lift line. Due to the dependence on the angular velocity by the linearized model, two harmonic motions were imposed as inputs in an unsteady aerodynamic simulation in UnPaM with a time step $\Delta t = 0.02$ s. A first harmonic variation of α was prescribed in UnPaM as

$$\begin{gathered}\alpha(t) = \alpha_0 + \Delta\alpha\, sin(\Omega\, t),\\ \beta(t) = \beta_0,\end{gathered} \tag{8}$$

with $\Delta\alpha = 1°$ and $\Omega = 1$ rad/s, that results in a period of 2π s. The UnPaM simulation was run for 2 complete periods obtaining the evolution of the force and moment coefficients. The first period was discarded to avoid transient states due to wake formation and initialization of UnPaM. To build the linearized model in Eq. (7) and obtain the aerodynamic derivatives in Table IV, this first harmonic motion was used to perform a linear fitting of the longitudinal aerodynamic coefficients $C_X(\alpha), C_Z(\alpha)$ and $C_m(\alpha, q)$, with $q = \dot{\alpha}\frac{c}{V_{Ref}}$ and $\dot{\alpha}$ computed analytically from Eq. (8). A second harmonic variation was imposed on β as

$$\begin{gathered}\alpha(t) = \alpha_0,\\ \beta(t) = \beta_0 + \Delta\beta\, sin(\omega\, t),\end{gathered} \tag{9}$$

with $\Delta\beta = 1°$ and the same period as in the first harmonic motion. In this case, the lateral-directional aerodynamic coefficients $C_Y(\beta), C_l(\beta, p)$ and $C_n(\beta, r)$ were fitted with $p = \frac{\dot{\beta}\sin(\alpha)\, b}{2\, V_{Ref}}$ and $r = \frac{-\dot{\beta}\cos(\alpha)\, b}{2\, V_{Ref}}$ (find more details about the kinematic inputs of UnPaM in Ref. [21]).

Figure 4 shows a comparison of the aerodynamic coefficients versus the angle of attack and sideslip angle computed with UnPaM and the linearized analytical model for the two harmonic motions prescribed in Eqs. (8-9). The start point for UnPaM's results is also represented with a red circle to track the evolution of UnPaM's coefficients as α and β vary. The three force coefficients (C_X, C_Y, C_Z) were modelled as steady, i.e., only dependent on the angle of attack or sideslip angle. This is the reason why the linearized model does not capture the unsteady variations but the average values during the harmonic motion. The reason behind this is the inability of the potential-flow model to properly capture typical stall-related hysteresis during unsteady variations of the angle of attack as demonstrated in Ref. [29]. Therefore, the dependence on the angular velocity was removed to avoid spurious results. On the other hand, the fitting of the three moment coefficients (C_l, C_m, C_n) is quasi-steady, i.e., dependent on α, β and the angular velocity. The linearized model of these three coefficients captures most of the unsteady variations predicted by UnPaM as shown in Fig. 4 (lower plots).

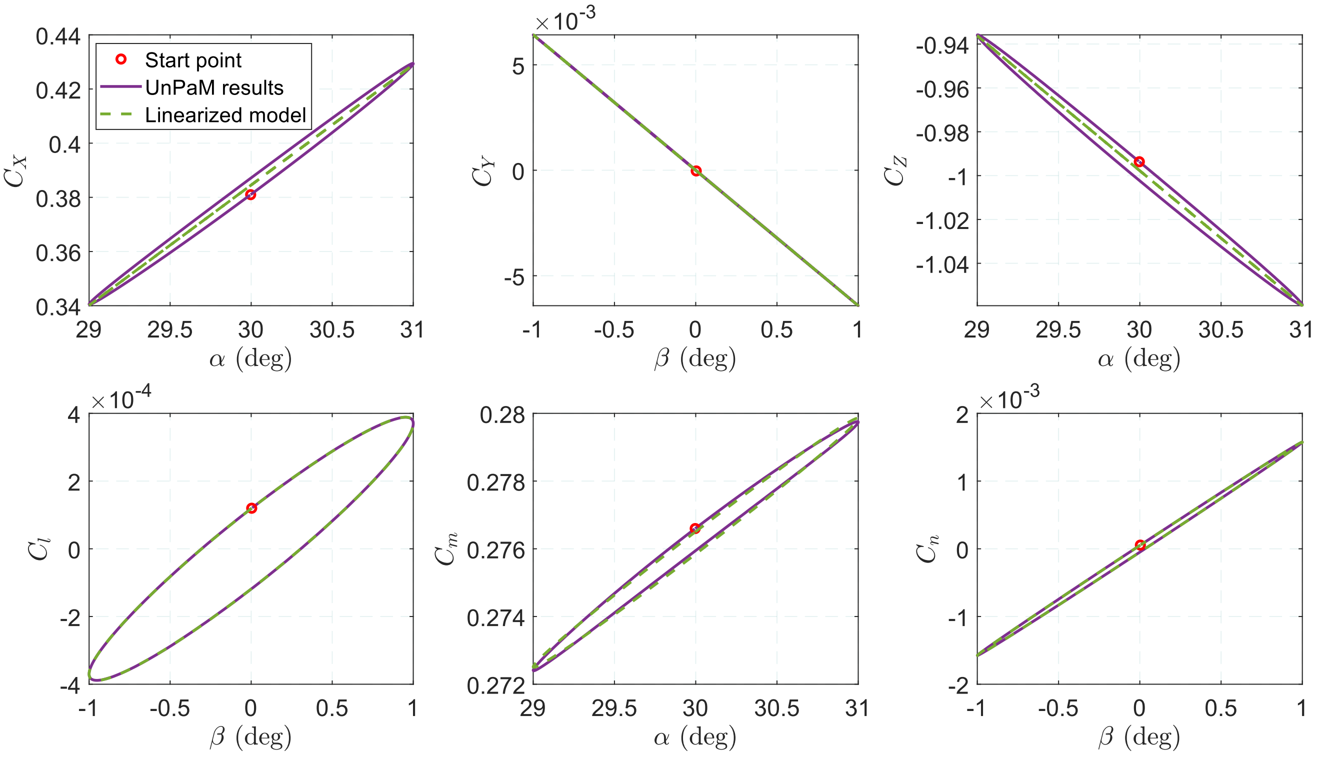

Fig. 4. Aerodynamic coefficients versus the angle of attack or sideslip angle computed with UnPaM and the linearized analytical model during for the harmonic motions in Eqs. (8-9).

2.3 Trim and stability analysis using bifurcation methods and numerical continuation

The kite's equilibrium and limit cycle responses are found numerically using the Dynamical Systems Toolbox (DST) [22], which is a MATLAB implementation of the numerical continuation software AUTO [23]. DST utilises a path-following algorithm to find, for a given control vector $\boldsymbol{x_c}$ and a user-defined parameter λ, the values of $\boldsymbol{x_s}$ that satisfy the conditions for either equilibrium (indicating trim)

$$\boldsymbol{f}(\boldsymbol{x_s}, \boldsymbol{x_c}, \lambda) = 0, \tag{10}$$

or, for limit cycles:

$$\boldsymbol{x}_s(t) = \boldsymbol{x}_s(t+T), \tag{11}$$

where $\boldsymbol{x}_s(t)$ denotes the value of the state vector at an arbitrary time t, and T is the period of the limit cycle. Equilibrium states need a constant control vector. λ is a user-defined parameter of interest for conducting a parameter sweep that is commonly named the bifurcation or continuation parameter. Once a solution is found, stability is determined by analysing the eigenvalues of the Jacobian of the flow $\boldsymbol{f}$ (evaluated at the equilibrium solutions) or the eigenvalues (Floquet multipliers) of the monodromy matrix (for limit cycles).

The continuation routine requires the user to supply a known solution to initialise the solver. This can be done by time-integrating the system with a set of input $\boldsymbol{x}_c$ until $\boldsymbol{x}_s$ settles onto its steady-state response, assuming that the steady state is stable and the initial condition belong to its basis of attraction. In our analysis we found equilibrium states and periodic orbits as a function of a bifurcation parameter that can be a physical parameter, like the wind speed, kite mass, tether attachment point, etc, or a parameter inside the control vector $\boldsymbol{x}_c$. The results are plotted on a bifurcation diagram, where the bifurcation parameter is shown on the horizontal axis and one of the state variables on the vertical axis.

In the published KiteElastic3 model [25], four states representing quaternions are used to describe the kite's orientation with respect to the Earth axis. When implemented into the continuation solver, these four quaternion states must be rewritten into four Euler angles states ϕ (roll), θ (pitch), and $\sin\psi$ and $\cos\psi$ representing yaw angle ψ. One reason is that for the same limit cycle response, quaternion states have twice longer periods than their Euler angle counterparts due to quaternions' double cover property. This longer period can cause numerical issues for the continuation solver. In addition, the yaw angle state should be split into $\sin\psi$ and $\cos\psi$ as explained in the appendix of [30].

3 Results and discussion

3.1 Effect on wind speed on trim points

Consider the trim point A with parameters listed in Table V. This results in a symmetric (lateral and directional states are null) but unstable trim at a height of 94.1 m. The kite's roll angle ϕ in this trim condition is zero depicted in Fig. 5. If no stabilising control input is provided, the kite flips over and eventually settles on an upside-down condition ($\phi = 180°$) at negative height. The transient motion between the two trim points suggests an unstable pendulum mode. Note that this trajectory would be unrealistic in a real AWE system, unless the ground station is located at a height above zero.

Table V. Parameters of the labelled points on trim diagrams.

Label	Wind	D_{LR}	L_C	ΔL_P	ΔL_S	Stability	Roll angle
A	8 m/s	0.7 m	100 m	0.4 m	0 m	Unstable equilibrium	0°
A'	8 m/s	0.7 m	100 m	0.4 m	0 m	Stable equilibrium	180°
B	8 m/s	7 m	100 m	0.4 m	0 m	Stable equilibrium	0°

The impact on wind speed on trim can be investigated by setting the wind speed as the continuation parameter. Fig. 6 shows two bifurcation diagrams depicting how the angle of attack and height at trim vary with different wind speeds. The main panels (a) and (b) show results within the aerodynamic data range of 20° to 40° angle of attack. In addition, two insets are provided to depict results at higher α ranges. These results may not be representative of the real kite but provide a fair comparison to some previous studies, which relied on simple aerodynamic modelling approaches. It can be seen from Fig. 6 that:

- Faster wind raises the trim point to a higher height while lowering the angle of attack.
- The kite requires at least 4.4 m/s of wind to fly, as no equilibrium solution exists below that speed.
- At low wind speeds near the minimum flyable value, a small region with three possible trim points exists as shown in the insets. The shape of the trim curve in this region resembles those presented in previous studies on simplified models [3, 5, 7]. However, unlike in [3, 5, 7], no stable solution exists in Fig. 6 due to the presence of the unstable lateral/directional dynamics that flips the kite upside down. It is expected that parts of the curve in Fig. 6 will become stable if the pitch dynamics can be isolated.
- A separate stable branch exists within the same wind speed range but with roll angle ϕ equals to 180° – corresponding to upside down flight at negative height. Since this flight regime is unphysical, it is not investigated further in this paper.

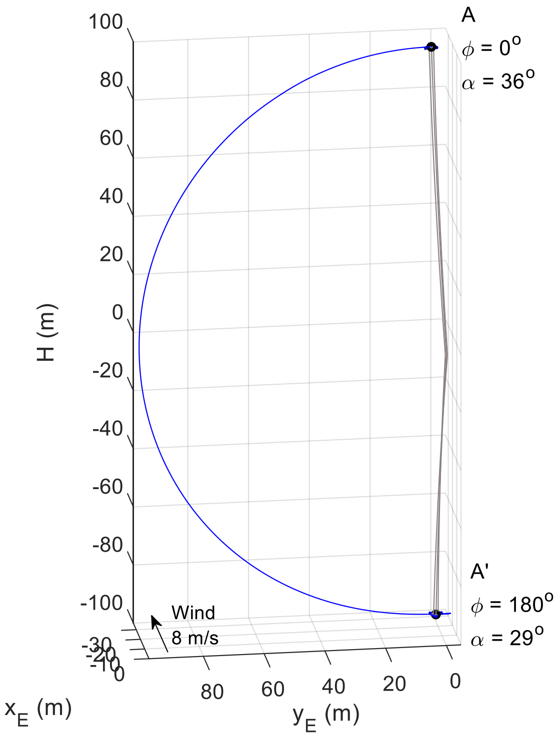

Fig. 5. Transition from unstable (positive height) trim to stable trim (negative height). The trajectory is shown in blue. Note that ϕ is the roll angle.

A notable observation from Fig. 6 is that as the wind speed reduces toward the minimum flyable speed, the height drop is relatively gradual: from 94.1 m at 8 m/s wind to 91.4 m at 6 m/s. However, once the wind speed drop below the minimum value at 4.4 m/s (noting that this is beyond the aerodynamic range), the kite suddenly does not generate enough lift to remain airborne. On the other hand, the change in angle of attack as wind speed reduces is more noticeable. This behaviour suggests that kite operators should keep track of not just the change in height, but also in the angle of attack, to prevent a crash.

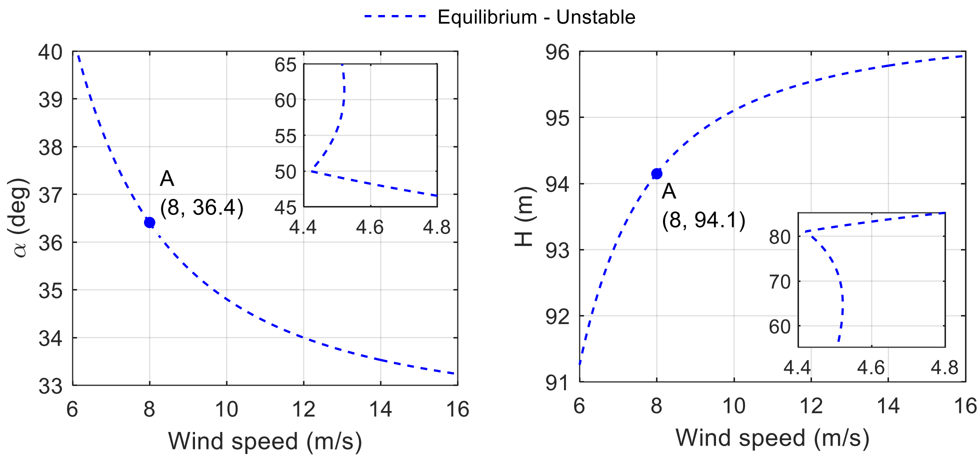

(a) (b)

Fig. 6. Effect of wind speed on angle of attack (a) and height (b) at trim with D_{LR} = 0.7 m.

3.2 Impact of the side tether anchor distance D_{LR} on stability

The lateral distance between the left and right two tether anchor points D_{LR} has a major effect on the stability of equilibrium solutions (see Fig. 3 for a reminder of D_{LR} definition). This link between D_{LR} and stability is illustrated in Fig. 7, noting that symmetric trim occurs at y_E = 0 m. Point A falls within the unstable equilibrium region as explained above. When D_{LR} reaches 6.2 m, a supercritical Hopf bifurcation appears, which indicates the presence of limit cycles at lower values of D_{LR}. The limit cycle branch is not fully shown in Fig. 7 due to difficulties encountered by the numerical continuation solver. However, time-integration of the dynamical system verifies that stable limit cycles exist for D_{LR} between 3.9 m and 6.2 m. The kite's trajectory in this region follows a figure-of-eight pattern, even though there is no active control input. Some of these trajectories are shown in Fig. 8. Also shown in Fig. 8 is a response at D_{LR} = 3 m, where the response is quasi-periodic (i.e, does repeat itself to form a closed orbit). These automatic figure of eight trajectory resembles the pendulum instability reported in Fig. 17 of [6], despite the differences in the dynamic model (constrained 5 DoF with no tether dynamics in [6] vs 6 DoF with tether dynamics in this work) and aerial platform used (inflatable fixed-wing aircraft vs delta kite). Therefore, both results suggest that this sideways oscillation is a possible dynamic mode of tethered kite systems with interesting applications to power generation since no control is needed to perform a typical AWE manoeuvre. Reducing D_{LR} further will destroy the automatic figure of eight response, and the kite converges to the upside-down trim point with negative height, as seen in Fig. 5.

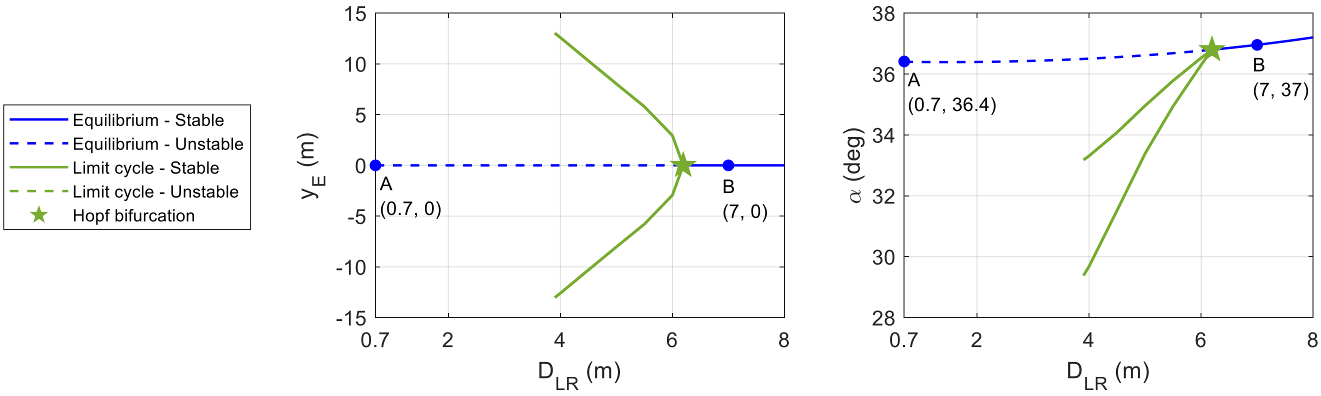

(a) (b)

Fig. 7. Effect of changing the tether anchor distance on the *Y*-coordinate (a) and angle of attack (b) at trim.

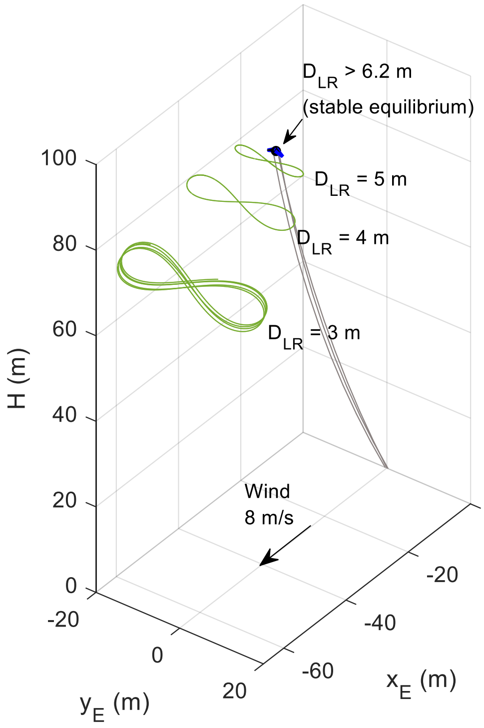

Fig. 8. 'Automatic' figure-of-eight trajectories: two as stable limit cycle and one as quasi-periodic limit cycle.

The equilibrium point becomes stable when D_{LR} increases beyond the Hopf bifurcation at 6.2 m. For completeness, a wind-speed sweep at symmetric trim was conducted at D_{LR} = 7 m that is shown in Fig. 9. Point B in this figure has the same parameters as point A in Fig. 6, except for D_{LR}. In both instances, the curves have similar shapes and numerical values, with the only difference being stability. Therefore, both wind speed and tether anchor distance D_{LR} contribute to kite stability.

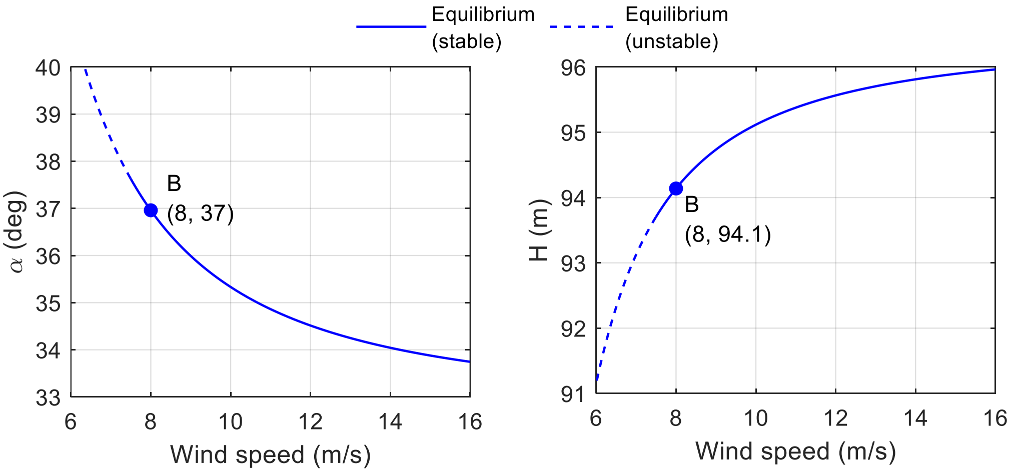

(a) (b)

Fig. 9. Effect of wind speed on angle of attack (a) and height (b) at trim at D_{LR} = 7 m.

Although increasing D_{LR} improves stability at trim, doing so reduces lateral controllability. Fig. 10 shows the lateral displacement from trim and the yaw angle response to the same differential tether length input but at two different D_{LR} configurations. Within the same 3-second window, the kite with low tether anchor distance achieves a larger lateral and yaw displacement, thereby having higher turning performance. Therefore, ground station design must consider the trade-off between stability at trim and lateral controllability required for manoeuvring.

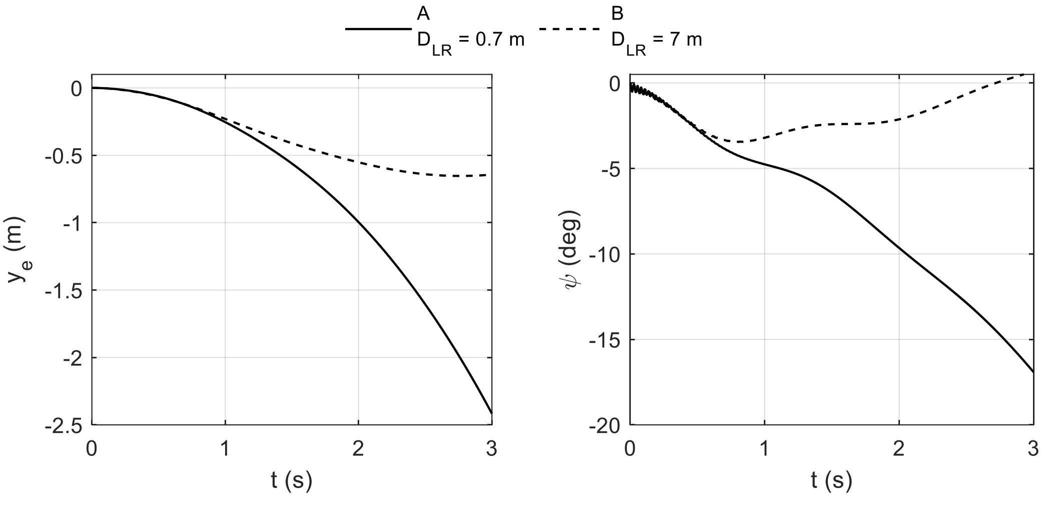

(a) (b)

Fig. 10. Lateral and directional responses to a step in differential tether input of amplitude ΔL_S = 0.01 m. The initial conditions are equilibrium trim at operating points A and B.

4 Conclusions

This paper has demonstrated the potential of bifurcation methods for analysing flight dynamics characteristics of high-fidelity AWE simulations, which often involve a large number of states. Key results from the KiteElasic3 model – developed on top of the LAKSA simulation package – include the co-existence of multiple solutions and self-excited figure-of-eight trajectories. These behaviours were observed under simple changes to anchor locations and wind speeds, which highlight the complex dynamics of three-line kite systems and verify results from previous studies that used simpler models. The influence of tether anchor location on the automatic figure-of-eight flight serves as one example of how bifurcation can be incorporated into the AWE system design process to satisfy stability and control requirements. Lastly, due to the large number of states in the simulation used (193), this paper does not discuss the modal characteristics of the kite motion as seen in [4, 31]. The link between these modes and dynamic stability is a potential topic for future work.

Acknowledgments

Duc H. Nguyen and Mark H. Lowenberg are supported by the UK's Engineering and Physical Science Research Council (EPSRC), grant number EP/Y014545/1. Francisco DeLosRíos-Navarrete is supported by the Comunidad de Madrid, grant number IND2022/AMB-23521. Francisco DeLosRíos-Navarrete, Jorge González-García, Iván Castro-Fernández, and Gonzalo Sánchez-Arriaga are supported by project PID2022-141520OB-I00 funded by MICIU/AEI/10.13039/501100011033.

References

[1] Cherubini, A., Papini, A., Vertechy, R., and Fontana, M. "Airborne Wind Energy Systems: A review of the technologies", *Renewable and Sustainable Energy Reviews,* Vol. 51, 2015, pp. 1461-1476. doi: 10.1016/j.rser.2015.07.053

[2] Khurshid, Y., Paul, P., Elhesasy, M., Ali, B., Kamra, M. M., Okasha, M., and Dief, T. N. "From inception to commercialization: A systematic review of airborne wind energy systems", *Sustainable Energy Technologies and Assessments,* Vol. 83, 2025, p. 104623.
doi: 10.1016/j.seta.2025.104623

[3] Adomaitis, R. A. "Kites and Bifurcation Theory", *SIAM Review,* Vol. 31, No. 3, 1989, pp. 478-483.
doi: 10.1137/1031092

[4] Sánchez, G. "Dynamics and Control of Single-Line Kites", *The Aeronautical Journal,* Vol. 110, No. 1111, 2006, pp. 615-621.
doi: 10.1017/S0001924000001470

[5] Snyder, I., Cairncross, R., Bland, G., and Stout, D. "Using Measured Aerodynamic Coefficients to Predict Pitch Equilibrium of Kites", *Journal of Aircraft,* Vol. 62, No. 4, 2025, pp. 1060-1066.
doi: 10.2514/1.C038138

[6] Terink, E. J., Breukels, J., Schmehl, R., and Ockels, W. J. "Flight Dynamics and Stability of a Tethered Inflatable Kiteplane", *Journal of Aircraft,* Vol. 48, No. 2, 2011, pp. 503-513.
doi: 10.2514/1.C031108

[7] Alexander, K., and Stevenson, J. "Kite equilibrium and bridle length", *The Aeronautical Journal,* Vol. 105, No. 1051, 2001, pp. 535-541.
doi: 10.1017/S0001924000017991

[8] Sánchez-Arriaga, G., García-Villalba, M., and Schmehl, R. "Modeling and dynamics of a two-line kite", *Applied Mathematical Modelling,* Vol. 47, 2017, pp. 473-486.
doi: 10.1016/j.apm.2017.03.030

[9] Koenemann, J., Sieberling, S., and Diehl, M. "OpenAWE: An Open Source Toolbox for the Optimization of AWE Flight Trajectories", *Airborne Wind Energy Conference 2017*, pp. 74, 2017.

[10] Jonkman, J., Hayman, G., Mudafort, R., Damiani, R., and Wendt, F. "*KiteFAST (GitHub despository)*", github.com/OpenFAST/KiteFAST [retrieved 18 January 2026].

[11] Listov, P., and Jones, C. "*OpenKITE (GitHub despository)*", github.com/PREDICT-EPFL/openkite [retrieved 18 January 2026].

[12] Sánchez-Arriaga, G., Pastor-Rodríguez, A., Sanjurjo-Rivo, M., and Schmehl, R. "A lagrangian flight simulator for airborne wind energy systems", *Applied Mathematical Modelling,* Vol. 69, 2019, pp. 665-684.
doi: 10.1016/j.apm.2018.12.016

[13] Eijkelhof, D., and Schmehl, R. "Six-degrees-of-freedom simulation model for future multi-megawatt airborne wind energy systems", *Renewable Energy,* Vol. 196, 2022, pp. 137-150.
doi: 10.1016/j.renene.2022.06.094

[14] De Schutter, J., Leuthold, R., Bronnenmeyer, T., Malz, E., Gros, S., and Diehl, M. "AWEbox: An Optimal Control Framework for Single- and Multi-Aircraft Airborne Wind Energy Systems", *Energies,* Vol. 16, No. 4, 2023, p. 1900.

[15] Allgaier, N., and Breipohl, F. "Markets of a 100 kW-AWE-System and EnerKíte's Pilot-Projects for a Perfect Market Entry", *Airborne Wind Energy Conference 2024*, pp. 2024.

[16] Castro-Fernández, I., Sánchez-Arriaga, G., and García-Villalba, M. "A review of the aerodynamics of airborne wind energy systems", *Progress in Aerospace Sciences,* Vol. 161, 2026, p. 101157.
doi: 10.1016/j.paerosci.2025.101157

[17] Williams, P., Sieberling, S., and Ruiterkamp, R. "Flight Test Verification of a Rigid Wing Airborne Wind Energy System", *2019 American Control Conference (ACC)*, pp. 2183-2190, 2019.
doi: 10.23919/ACC.2019.8814338

[18] Bosch, A., Schmehl, R., Tiso, P., and Rixen, D. "Dynamic Nonlinear Aeroelastic Model of a Kite for Power Generation", *Journal of Guidance, Control, and Dynamics,* Vol. 37, No. 5, 2014, pp. 1426-1436.
doi: 10.2514/1.G000545

[19] Gaunaa, M., Li, A., McWilliam, M., and Kelly, M. "Lifting-Line Aerodynamics for Airborne Wind Energy on a Prescribed Path", *10th International Airborne Wind Energy Conference (AWEC 2024)*, Paper 2024.
doi: 10.4233/uuid:85fd0eb1-83ec-4e34-9ac8-be6b32082a52

[20] Sánchez-Arriaga, G., and Pastor-Rodríguez, A. "*LAgrangian Kite SimulAtors (LAKSA)*", github.com/UC3M-AWE/laksa [retrieved 27 September 2025].

[21] Castro-Fernández, I., Borobia-Moreno, R., Cavallaro, R., and Sánchez-Arriaga, G. "Three-Dimensional Unsteady Aerodynamic Analysis of a Rigid-Framed Delta Kite Applied to Airborne Wind Energy", *Energies,* Vol. 14, No. 23, 2021, p. 8080.
doi: 10.3390/en14238080

[22] Coetzee, E., Krauskopf, B., and Lowenberg, M. H. "The Dynamical Systems Toolbox: Integrating AUTO into Matlab", *16th US National Congress of Theoretical and Applied Mechanics*, USNCTAM Paper USNCTAM2010-827, 2010.

[23] Doedel, E. J., and Oldeman, B. E. "*AUTO-07P GitHub depository*", github.com/auto-07p/auto-07p [retrieved 1 March 2025].

[24] Ríos-Navarrete, F. d. l., Castro-Fernández, I., Cavallaro, R., and Sánchez-Arriaga, G. "Experimental validation of an airborne wind energy simulator based on a semi-empirical aerodynamic model", *Wind Energy Science Conference (WESC 2023)*, Paper 2023.
doi: 10.5281/zenodo.8086316

[25] Ríos-Navarrete, F. d. l., and Castro-Fernández, I. "*KiteElastic3*", github.com/UC3M-AWE/laksa/tree/master/src/KiteElastic3 [retrieved 19 March 2026].

[26] Sánchez-Arriaga, G., Serrano-Iglesias, J. A., Leuthold, R., and Diehl, M. "Modeling and Natural Mode Analysis of Tethered Multi-Aircraft Systems", *Journal of Guidance, Control, and Dynamics,* Vol. 44, No. 6, 2021, pp. 1199-1210.
doi: 10.2514/1.G005075

[27] Navarrete, F. d. l. R. "Ground-Actuated Airborne Wind Energy System Demonstrator", PhD thesis, Aerospace Engineering, Universidad Carlos III of Madrid, Madrid, Spain, 2025.

[28] Cavallaro, R., Nardini, M., Demasi, L., and Santarpia, E. "Amphibious PrandtlPlane: Preliminary Design Aspects Including Propellers Integration and Ground Effect", *56th AIAA/ASCE/AHS/ASC Structures, Structural Dynamics, and Materials Conference*, AIAA Paper AIAA 2015-1185, 2015.
doi: 10.2514/6.2015-1185

[29] Castro-Fernández, I., Cavallaro, R., Schmehl, R., and Sánchez-Arriaga, G. "Unsteady Aerodynamics of Delta Kites for Airborne Wind Energy Under Dynamic Stall Conditions", *Wind Energy,* Vol. 27, No. 9, 2024, pp. 936-952.
doi: 10.1002/we.2932

[30] Nguyen, D. H., Lowenberg, M. H., and Oland, E. "Trimming a rigid-wing airborne wind system for coordinated circular flights", *Wind Energy Science,* Vol. 11, No. 1, 2026, pp. 285-298.
doi: 10.5194/wes-11-285-2026

[31] Losantos, L. S., and Sánchez-Arriaga, G. "Flight Dynamics and Stability of Kites in Steady and Unsteady Wind Conditions", *Journal of Aircraft,* Vol. 52, No. 2, 2015, pp. 660-666.
doi: 10.2514/1.C032825